Spectral Reconstruction from Dispersive Blur: A Novel Light Efficient Spectral Imager

Yuanyuan Zhao*,1 Xuemei Hu*,1 Hui Guo[1] Zhan Ma[1] Tao Yue[1,2] Xun Cao[1]
[1]Nanjing University, Nanjing, China
[2]NJU institute of sensing and imaging engineering, Nanjing, China
{yuan_square, guo_hui}@smail.nju.edu.cn {xuemeihu, mazhan, yuetao, caoxun}@nju.edu.cn

Abstract

Developing high light efficiency imaging techniques to retrieve high dimensional optical signal is a long-term goal in computational photography. Multispectral imaging, which captures images of different wavelengths and boosting the abilities for revealing scene properties, has developed rapidly in the last few decades. From scanning method to snapshot imaging, the limit of light collection efficiency is kept being pushed which enables wider applications especially under the light-starved scenes. In this work, we propose a novel multispectral imaging technique, that could capture the multispectral images with a high light efficiency. Through investigating the dispersive blur caused by spectral dispersers and introducing the difference of blur (DoB) constraints, we propose a basic theory for capturing multispectral information from a single dispersive-blurred image and an additional spectrum of an arbitrary point in the scene. Based on the theory, we design a prototype system and develop an optimization algorithm to realize snapshot multispectral imaging. The effectiveness of the proposed method is verified on both the synthetic data and real captured images.

1. Introduction

The spectrum of light contains rich information of the scene, and is of great significance for many applications, e.g., medical diagnostics [3], object distinguishment [8], face recognition [26], etc. The core technique for capturing the spectrum of light is snapshot multispectral imaging, i.e., taking images or videos of different wavelength band over the visible wavelength range in a single snapshot.

Existing snapshot multispectral imaging techniques can be mainly categorized into five main categories: tomography methods [9], remapping methods [7, 13, 16], coded aperture methods [11, 17, 23, 28, 30], spectral filter based methods [5, 21, 22, 25] and RGB camera based methods [1, 2, 4, 10, 33]. The total light throughput of these multispectral imaging techniques is sacrificed either in the spatial or the spectral dimension, which greatly reduce the signal-to-noise-ratio (SNR) of measurements and prevent the high-quality multispectral reconstruction [24]. Thus, improving the light throughput is one of the key concern in spectrometer design, especially for the video-rate spectral imagers where the exposure time is strictly limited.

In this paper, we propose a novel snapshot multispectral imaging technique with high light throughput. Based on the difference of blur (DoB) constraints [12] (i.e., the derivative of the dispersive blur along the dispersive direction over each edge is exactly the difference of spectrum of the adjacent area, as shown in Fig. 1(b)), we theoret-

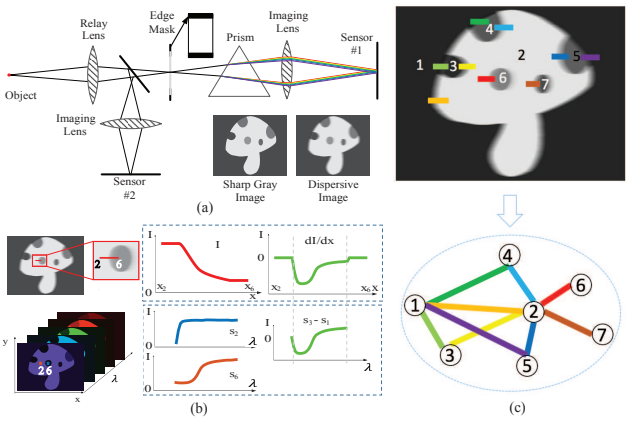

Figure 1. Overview of our imaging method. (a) Prototype system: incoming light is splitted into two light paths: a sharp gray image is captured from one light path for the location information of edges. A dispersive-blurred and margin-masked image is captured on the other path for the DoB constraints and the additional spectrum of the edge point. (b) DoB constraints along each edge: the derivative of the dispersive blur along each edge equals the difference of the spectrum of the adjacent areas. (c) DoB constraints over all edges constitute a graph, based on which we reconstruct the hyperspectral images.

*Both authors contributed equally to this work.

ically prove that we can recover the multispectral images from a single dispersive-blurred image plus an additional spectrum of a single point in the scene. Specifically, the multispectral image reconstruction problem can be modelled as a N-linear equation system, and through introducing a graph model, we theoretically prove that DoB constraints provide only $N-1$ independent constraints and the spectrum of an additional point is required for multispectral recovery. We propose to introduce the edge mask to get an additional spectrum of the edge point and realize the full rank retrieval of multispectral images. Based on the theory we proved, we design a snapshot multispectral imaging technique (Fig. 1(a)) that could capture all the required information. The imager is composed of two light paths: the dispersive-blurred path is for capturing the above mentioned full rank multispectral information and the gray-camera path is for locating the sharp edge. An optimization algorithm is proposed to reconstruct the multispectral information from the captured two images. Since the light throughput loss introduced around the edge is ignorable, our methods could achieve snapshot multispectral imaging with a high light efficiency.

High throughput imaging could directly improve the SNR of the measurements, and improve the following hyperspectral recovery, which is especially important in the light-starved applications such as multispectral fluorescence microscopic imaging [20], high speed multispectral imaging [31] and plenoptic light imaging techniques [32, 34], etc. Besides, other than the spectral domain imaging, the theory and imaging method we proposed for extracting the information from dispersion could be applied to the other domain, such as time domain, and enables high-throughput snapshot ultrafast imaging [14].

In particular, we make the following contributions:

- We *prove* theoretically that we can recover the multispectral images from a single dispersive-blurred image plus the spectrum of an additional point in the scene based on the graph theory.
- We *develop* a pixel-wise spectral reconstruction algorithm based on the proposed theory.
- We *build* a prototype imaging system to verify this approach and *demonstrate* the feasibility and effectiveness with both synthetic and experimental data.

2. Related Work

Traditional multispectral imaging are implemented through scanning either along the spatial dimension [6, 27] or along the spectral dimension [15]. These scanning methods are slow and the optical throughput is quite low, which is not applicable for realtime multispectral imaging especially under light-starved conditions [14, 20, 31]. Snapshot spectrometer collect the three dimensional multispectral image in a single exposure period, with a much higher optical throughput than scanning based methods [18]. Researches in this field has been evolving rapidly in the last few decades, which can be mainly categorized into five main methods.

Computed Tomography Methods. Descour and Dereniak [9] proposed the Computed Tomography Imaging Spectrometer (CTIS) and reconstruct the multispectral images from a set of dispersive projections. Assuming the number of projection is N_{p}, the spatial resolution captured is reduced to $1/N_{\mathrm{p}}$ of the sensor pixel number N and so as the optical throughput. Instead of capturing multiple projections in different directions, we proposed to capture the multispectral images with only one dispersive projection, thus with a much higher light efficiency.

Remaping Methods. Remapping methods are proposed to remap the 3D multispectral volume to 2D spatial detection [7, 13, 16]. The spatial information is directly sacrificed in exchange of spectral resolution, i.e., assuming that the spectral resolution is N_λ, the total optical throughput of the multispectral imaging is reduced to $1/N_\lambda$. While in our method, the spectral information all over the image are dispersively blurred and integrated together, no spatial information are directly sacrificed and we experimentally demonstrate that our method could preserve most of the space information with the proposed algorithm.

Coded Aperture Methods. To overcome the spatial-spectral resolution trade-offs, methods combing compressive sensing and the statistical priors of natural multispectral images are proposed [11, 17, 23, 28, 30] , through introducing random-amplitude aperture to codes both the spatial and the spectral dimension. These coded aperture based methods enable multispectral imaging with high spatial resolution, while the loss of optical throughput introduce by the random coded aperture is 50% percent and the optical system of these methods require complex calibration while our method only requires simple calibration between the dispersive light path and the sharp gray light path.

Spectral Filter Based Methods. To capture the multispectral images with a compact imaging system, a set of spectral filter array (SFA) based methods with modulations either in the primal domain [5, 22, 25] or in the Fourier domain [21] are investigated. Benefiting from the computational reconstruction, these methods use wide-band spectral filters and thus can achieve even more than 50% light throughput. But generally the manufacturing of SFAs is difficult and thus limits their widely application in practice.

RGB Camera based Methods. Recently, RGB imaging sensors are explored to recover the multispectral images [1, 2, 4, 10, 33]. While these methods can realize multispectral with RGB cameras, the RGB Bayer filter blocks a large part of the light and is light inefficient.

In all, we propose a novel multispectral imaging methods in this paper, which only requires to capture a single disper-

sive blurred image and a sharp gray image. Our imaging system is easy to calibrate, of low cost and light efficient. With our snapshot spectral imaging technique, we could capture high SNR measurements of multispectral data and we demonstrate that our method could achieve state-of-the-art snapshot multispectral imaging.

3. Theory

In this part, we will introduce the proposed theory for multispectral imaging and recovery. Our theoretical inference is based on two assumptions: 1) The image can be explicitly segmented into a series of regions, and the spectra are uniform up to a scale factor in each region. 2) All the maximum distance between each pair of adjacent edges along the dispersive direction are larger than the size of dispersion. We need to note that the first assumption are only invalid in the scene where there are specularities or complex illumination, which is not the research focus of this paper. As for the second assumption, in most cases, the edges of the narrow region are not exactly parallel, the information is mixed inconsistently, where heterogeneous information contained in the edges along the narrow regions can still guarantee the high fidelity spectral recovery, as will be further demonstrated in the experimental part.

To simplify the derivation, we consider the case without shading effect first and discuss the effect introduced by shading later. Without shading, natural images consisted of a set of surfaces with unified spectral reflectance are considered first. We will show that DoB constraints can provide most of the spectral information for recovering the entire multispectral image, except a single additional spectrum of an arbitrary point is required.

3.1. DoB Constraints

In 1989, Funt and Ho [12] have pioneeringly proposed to estimate the difference of spectra from image edges. To facilitate further inference, we first briefly introduce this DoB constraints. According to the principle of dispersion, the spectrum of a single point will spread spatially when passing the dispersive elements, generating a spectral dispersion band $\mathbf{s}$, which maps the spectrum into spatial domain. Considering an edge between two regions $(i,\ j)$ with two different spectral dispersion band $(\mathbf{s}_i, \mathbf{s}_j)$, the DoB constraints can be represented as:

$$\nabla_\theta \mathbf{b} = \delta_{ij} * (\mathbf{s}_i - \mathbf{s}_j), \tag{1}$$

where δ_{ij} is the impulse function, indicating the edge location between regions i and j, $*$ denotes spatial convolution, $\nabla_\theta \mathbf{b}$ represent the derivative of the image intensity $\mathbf{b}$ at the edge along the projection angle θ. Thus, if we know the position δ_{ij} of the edge, we can derive the difference of the spectra $\mathbf{s}_i$ and $\mathbf{s}_j$ from the derivative of the dispersive blur.

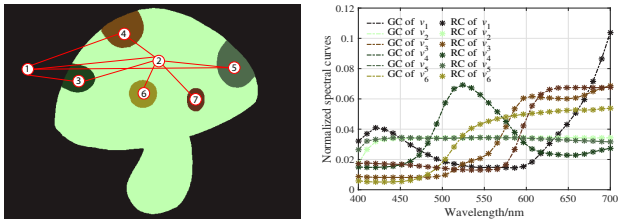

(a) (b)

Figure 2. Illustration of the graph model and verification on synthetically generated image. The 'mushroom' multispectral image in Fig. 1(b) is used to synthesize the sharp gray image and the dispersive image, which is dispersively blurred on $x-$ direction. (a) The corresponding graph model. (b) The reconstructed spectral curves (RC) as well as the ground truth spectral curves (GC) of the surface pieces indexed in (a).

For a dispersive blurred image, we could define an edge matrix $\mathbf{A}$ and DoB matrix $\mathbf{B}$ to represent the DoB constraints. Mathematically, we use each row of $\mathbf{A}$ and $\mathbf{B}$ to denote a DoB constraint of an edge. All the DoB constraints of the entire dispersive blurred image can be formulated by

$$\mathbf{AS} = \mathbf{B}, \tag{2}$$

where $\mathbf{S} = [\mathbf{s}_1, \mathbf{s}_2, \ldots, \mathbf{s}_N]^T$ denote the spectra of regions $1, 2, \ldots, N$ in the image, each row of $\mathbf{A}$ has only two nonzero elements 1 and -1 which indicates the corresponding spectra $\mathbf{s}_i$ and $\mathbf{s}_j$ of the two surfaces beside the edge, each row of $\mathbf{B}$ is the derivative of blur at the edge. We will prove in the next section that $\mathbf{A}$ is of rank N-1, and an additional spectrum of a single point is required to realize full-rank recovery of $\mathbf{S}$.

3.2. Graph Theory for Spectrum Reconstruction

To facilitate discussing the rank of $\mathbf{A}$, we build a corresponding graph model $\mathcal{G} = (\mathcal{V}, \mathcal{E})$, where $\mathcal{V}$ is the vertex set and each vertex denote a single surface. $\mathcal{E}$ is the edge set and each edge denotes the adjacency between the corresponding vertexes. As in Fig. 2, by introducing the graph model, each row of $\mathbf{A}$ corresponds to an edge in $\mathcal{E}$. We use the undirected graph in this paper without loss of generality and since each of the surfaces in an image is at least adjacent to another surface, the undirected graph $\mathcal{G}$ is connected. Given the customized edge matrix $\mathbf{A}$ of a dispersive blurred image and its corresponding graph model $\mathcal{G}$, we have the following theorem.

Theorem 1 *The rank of the edge matrix* $\mathbf{A}$ *exactly equals to the edge number of the spanning tree of its corresponding undirected connected graph* $\mathcal{G}$.

Theorem 1 follows from Lemma 1 below which proves the equivalence of the connected graph $\mathcal{G}$ and its spanning tree $\mathcal{G}'$ for the spectrum reconstruction problem. According to

the characteristics of trees, a tree $\mathcal{G}'$ of N vertexes has $N-1$ edges, and thus its corresponding edge matrix $\mathbf{A}'$ has $N-1$ rows. In other words, the rank of $\mathbf{A}$ and $\mathbf{A}'$ is smaller than or equals to $N-1$. Meanwhile, according to Lemma 2, the edge matrix of a tree is of full row rank. Therefore, the rank of $\mathbf{A}'$ and the rank of $\mathbf{A}$ are both $N-1$.

Lemma 1 *A connected graph $\mathcal{G}$ and its spanning tree $\mathcal{G}'$ have the same spectrum solution space.*

Proof sketch of Lemma 1 We separate the lemma into the forward and backward propositions.
Forward proposition: any feasible solution $\mathbf{S}$ of graph model $\mathcal{G}$ is also a solution of $\mathcal{G}'$. Assume $\mathbf{A}$ and $\mathbf{B}$ are the corresponding edge matrix and the DoB matrix of the graph model $\mathcal{G}$, $\mathbf{S}$ is a solution of $\mathbf{AX}=\mathbf{B}$. The spanning tree $\mathcal{G}'$ of $\mathcal{G}$ can be derived by removing the edges which are parts of cycles while keeping the connection property. In other words, the edge matrix $\mathbf{A}'$ and the DoB matrix $\mathbf{B}'$ are pruned version of $\mathbf{A}$ and $\mathbf{B}$, and the removed rows just correspond to the removed edges. Therefore, the forward proposition here is self-evident since the solution space of $\mathcal{G}$ is exactly a subset of the solution space of $\mathcal{G}'$.
Backward proposition: any feasible solution $\mathbf{S}'$ of graph model $\mathcal{G}'$ is also a solution of $\mathcal{G}$. Since a removed edge e is a part of a certain cycle $\mathcal{C}$ in the original graph $\mathcal{G}$, it means that the rest edges of the cycle $\mathcal{C}\backslash e$ form a path connecting the vertexes of the end of the removed edge e. As the direction of the edges denote the direction of difference operation (from 1 to -1) and once a certain directed constraint is known, its reverse version can be easily derived by changing the sign of the elements of the corresponding row in $\mathbf{B}$, thus we can form a directed path from one end of the removed edge e to the other end, and the summation of the corresponding rows of $\mathbf{A}$ has two non-zero elements $1,-1$, which corresponds to the start and end vertexes respectively. This summed row vector exactly equals the removed edge e. Consequentially, the removed row of e can be linearly represented by the rest rows of $\mathcal{C}\backslash e$, so that the solution $\mathbf{S}'$ satisfies the constraints $\mathcal{C}\backslash e$ in graph $\mathcal{G}'$ also satisfies the constraint $\mathcal{C}=(\mathcal{C}\backslash e)\cup e$ in graph $\mathcal{G}$.

Lemma 2 *The edge matrix $\mathbf{A}$ of an undirected acyclic graph $\mathcal{G}$, a.k.a. a tree, is of full row rank.*

Proof sketch of Lemma 2 According to Lemma 1, the solution spaces of the given undirected acyclic graph $\mathcal{G}$ and its corresponding complete graph $\mathcal{G}^*$ (i.e., $\mathcal{G}^*$ has the same vertex set with $\mathcal{G}$, and every pair of distinct vertexes in $\mathcal{G}^*$ is connected by a unique edge) are exactly the same, that is because $\mathcal{G}$ can be regarded as a spanning tree of $\mathcal{G}^*$. Meanwhile, a chain graph $\mathcal{G}^c$ which is the subgraph of $\mathcal{G}^*$ and threads all the vertexes of $\mathcal{G}^*$ is as well a spanning tree of $\mathcal{G}^*$ and also share the same solution space of $\mathcal{G}^*$. Therefore, $\mathcal{G}$ and $\mathcal{G}^c$ have the same solution space as well. Furthermore, the edge matrix $\mathbf{A}^c$ of the chain graph $\mathcal{G}^c$ is an incomplete Toeplitz matrix which is of full row rank obviously. Since the chain graph $\mathcal{G}^c$ and $\mathcal{G}$ have the same solution space, $\mathbf{A}^c$ and $\mathbf{A}$ have the same solution space as well and thus both of them are of full row rank $(N-1)$.

3.3. Shading effect

Because of the illumination condition and the shape of the scenes, the light emitted from the different points of a same surface may have different irradiance. The uniform assumption ignores this shading effect and thus is incapable of dealing with the real scenes. In the following, we introduce the shading effect by using the irradiance scale model to make the proposed method more feasible for practical applications.

For the points of a certain surface, we assume that the reflectances are of the uniform spectrum up to a scale, which means that the observed spectrum of a certain pixel p in surface i is,

$$\mathbf{s}_p^o = I_p \overline{\mathbf{s}_i}, \tag{3}$$

where I_p is the illumination intensity integrated over all wavelength, $\overline{\mathbf{s}_i}$ is the normalized spectrum of surface i and $\mathbf{s}_p^o$ is the observed spectrum of pixel p in it, we could get

$$\nabla_\theta^{(p,q)}|_{p\in\mathrm{surf}(i),q\in\mathrm{surf}(j)}\mathbf{b} = \delta_{ij} * (I_p\overline{\mathbf{s}_i} - I_q\overline{\mathbf{s}_j}), \tag{4}$$

where (p,q) denote the adjacent pixels in surface i and j. $\nabla_\theta^{(p,q)}\mathbf{b}$ is the DoB constraint of pixel pair (p,q). For each adjacent surface pair i and j, there are many DoB constraints with different intensity pairs I_p and I_q. A set of constraints with different intensity elements I_p and I_q instead of 1 and -1 then replace each row of adjacent matrix $\mathbf{A}$. In most cases, when there are several different weighted constraints for a single surface pair, the matrix $\mathbf{A}$ becomes full-rank, and the problem is solvable. However, we found the condition number of $\mathbf{A}$ is not always small in practice, since the shading caused intensity change is insufficiently large to provide an additional well-defined constraint. Thus, we propose to introduce the spectrum of a single point to reduce the ill-posedness in practice.

Note that after introducing the irradiance scale model in Eq. 4, the number of unknowns increases from NM to $NM+P$, where P is the number of pixels. The added unknowns are the intensities of the sharp gray scale image. Although the sharp gray image can be retrieved from the dispersive blurred image by using blind deblurring algorithms, we propose to use the hybrid camera system as in [7] to directly capture the sharp gray image. Therefore, in the following experiment, we propose a multispectral imaging technique that could captures the sharp gray image, the dispersive blurred image and a single spectrum of a certain point in a snapshot way and verify the proposed theory.

4. Point-wise Reconstruction Algorithm

Based on the proposed theory, we propose a spectral imager as in Fig. 1(a): incoming light is splitted into two light paths capturing both the dispersive blurred image and the sharp gray image. To capture the required additional spectrum of a single point, we introduce a side block mask in the dispersive light path to cut off the sides of the virtual image focused on sensor #1. Thus the spectra of these blocked regions are known (i.e. zero for all spectral channels), and the full rank information for multispectral image reconstruction can be captured.

If the segmentation of scenes is given, the spectra of each surface can be reconstructed by solving Eq. 2. However, practically, computing exact segmentations is usually difficult for existing segmentation technologies. Therefore, in this subsection, we develop a pixel-wise reconstruction algorithm with two snapshot inputs, i.e. the dispersive blurred image and sharp gray image, to make the proposed method feasible in practice.

4.1. Problem Statement

Fidelity Term. Using the proposed system, we can capture dispersive blurred and sharp gray image pairs simultaneously, and the acquisition process can be denoted by

$$\begin{aligned} \mathbf{G} &= \mathbf{P}_g\mathbf{S} = \sum_{\lambda} \mathbf{S}(x, y, \lambda) \\ \mathbf{D} &= \mathbf{P}_d\mathbf{S} = \sum_{\lambda} \mathbf{S}(x + \Delta x(\lambda), y, \lambda), \end{aligned} \tag{5}$$

where $\mathbf{G}$ and $\mathbf{D}$ are the gray projection and dispersive projection of the multispectral cube $\mathbf{S}$. $\mathbf{P}_g$ and $\mathbf{P}_d$ are the projection matrix. x, y are the spatial coordinates and λ denotes wavelength. Given this projection model, the basic fidelity term of our reconstruction problem is derived,

$$E_f = ||\mathbf{G} - \mathbf{P}_g(\mathbf{S})||^2 + ||\mathbf{D} - \mathbf{P}_d(\mathbf{S})||^2, \tag{6}$$

where E_f denotes the fidelity term of our objective function, and $||\cdot||^2$ is the square of L-2 norm, which is usually applied for reconstruction problem.

DoB Constraint. Instead of segmenting input images into regions and extracting DoB constraints explicitly, we utilize the pixel-wise difference projection constraints to model the DoB constraints here,

$$E_{DoB} = ||\nabla_{x,y}\mathbf{D} - \mathbf{P}_d(\nabla_{x,y}\mathbf{S})||^2, \tag{7}$$

where $\nabla_{x,y}$ means the difference operation in both row x and column y directions. $\nabla_{x,y}\mathbf{S}$ is full of zeros except for the pixels on the edges, and the non-zero value on the edge along the spectral dimension is exactly the difference between the spectra of the adjacent surfaces. The dispersive projection operation shear the difference cube and project the differences on the edges of all the channels on the DoB plane. $\nabla_{x,y}\mathbf{D}$ denotes the difference map of dispersive blurred image, and thus exactly matches the DoB projections. This pixel-wise difference projection constraint formulates all the DoB constraints.

Side Block Constraint. We introduce the side block constraint to model the the marginal mask:

$$E_{side} = ||\mathbf{S} \odot \mathbf{M}||^2, \tag{8}$$

where $\mathbf{M}$ is the side block mask with 1 in the block areas and 0 in the rest, and $\odot$ denotes the pixel-wise product.

Cross-channel & Sparse Regularizer. The proposed method is essentially benefited from the piece-wise smooth assumption of natural scenes, and the segmentation is used to imply this assumption in the inferences in Sec.3. In our practical implementation, the cross-channel and sparse constraints are adopted to replace the explicit segmentation to reduce the ill-posedness of the problem. The cross-channel and sparse regularizer can enforce the piece-wise smoothness on spatial domain and similar edge locations on different spectral channels [19]. In our scenario, a sharp projection image is given, which can be used as the reference map for the cross-channel and sparse constraint,

$$E_{cs} = ||\nabla_{x,y}\mathbf{S}||_1 + \sum_{\lambda} ||\nabla_{x,y}\mathbf{S}_\lambda(x, y) - \nabla_{x,y}\mathbf{G}||_1, \tag{9}$$

where $||\cdot||_1$ is the L-1 norm, and $||\nabla_{x,y}\mathbf{S}||_1$ is the sparse term. $\sum_\lambda ||\nabla_{x,y}\mathbf{S}_\lambda(x, y) - \nabla_{x,y}\mathbf{G}||_1$ is the cross-channel term, and $\nabla_{x,y}\mathbf{S}_\lambda(x, y)$ is the gradient map of spectral channel $\mathbf{S}_\lambda$, $\nabla_{x,y}\mathbf{G}$ denotes the gradient map of sharp projection $\mathbf{G}$.

Objective Function. So far, we have all the fidelity and constraints of our multispectral reconstruction problem, and the final objective function becomes

$$E = E_f + \lambda_{DoB}E_{DoB} + \lambda_{side}E_{side} + \lambda_{cs}E_{cs}, \tag{10}$$

where λ_{DoB}, λ_{side} and λ_{cs} are the weights of corresponding terms respectively.

4.2. Optimization

To optimize Eq. 10, we first introduce an auxiliary variable $\mathbf{Q}_{cs}$ here,

$$\begin{aligned} E' =& E_f + \lambda_{DoB}E_{DoB} + \lambda_{side}E_{side} \\ &+ \beta_{cs}||\nabla\mathbf{S} - \mathbf{Q}_{cs}||^2 + \lambda_{cs}||\mathbf{Q}_{cs}||_1 \\ &+ \lambda_{cs}||\mathbf{Q}_{cs} - \nabla\mathbf{G}||_1. \end{aligned} \tag{11}$$

Then Eq. 11 can be solved by iteratively optimizing two sub-problems.

Q-subproblem. In this subproblem, we just optimize the $\mathbf{Q}_{cs}$ related terms and update the optimal $\mathbf{Q}_{cs}$ by fixing $\mathbf{S}$.

The sub-objective function becomes

$$E(\mathbf{Q}_{cs}) = \beta_{cs}||\nabla\mathbf{S} - \mathbf{Q}_{cs}||^2 + \lambda_{cs}||\mathbf{Q}_{cs}||_1 + \lambda_{cs}||\mathbf{Q}_{cs} - \nabla\mathbf{G}||_1. \quad (12)$$

Eq. 12 can be optimized in a pixel-wise way, which means the sub-objective function can be divided into a series of sub-functions $E(\mathbf{Q}_{cs}) = \sum_{(x,y)} E(\mathbf{Q}_{cs}(x,y))$, which takes only one single pixel into consideration,

$$E(\mathbf{Q}_{cs}(x,y)) = \beta_{cs}||\nabla\mathbf{S}(x,y) - \mathbf{Q}_{cs}(x,y)||^2 + \lambda_{cs}||\mathbf{Q}_{cs}(x,y)||_1 + \lambda_{cs}||\mathbf{Q}_{cs}(x,y) - \nabla\mathbf{G}(x,y)||_1. \quad (13)$$

To minimize Eq. 12 fast, we adopt the 2-D lookup table method in [36]. Specifically, the minimum $\mathbf{Q}_{cs}$ with different $\nabla\mathbf{S}(x,y)$ and $\nabla\mathbf{G}(x,y)$ are recorded. In practice, both $\nabla\mathbf{S}(x,y)$ and $\nabla\mathbf{G}(x,y)$ are uniformly sampled from -1 to 1 with interval 0.002. For each combination of $\nabla\mathbf{S}(x,y)$ and $\nabla\mathbf{G}(x,y)$, the minimum $\mathbf{Q}_{cs}$ are computed numerically. By generating the 2-D lookup table before hand, we can solve the Q-subproblem efficiently.

S-subproblem. Then, the spectral cube $\mathbf{S}$ is updated in S-subproblem. The terms related to $\mathbf{S}$ are

$$E(\mathbf{S}) = E_f + \lambda_{DoB}E_{DoB} + \lambda_{side}E_{side} + \beta_{cs}||\nabla\mathbf{S} - \mathbf{Q}_{cs}||^2. \quad (14)$$

It is obvious that all the terms in Eq. 14 are quadratic terms, and thus can be easily solved by gradient based optimization algorithm. In our implementation, the Conjugate Gradient (CG) algorithm is used to optimize Eq. 14.

5. Assessment

In this section, the proposed method is verified on various scenes, including both synthetic and real captured data. Both quantitative and qualitative comparisons with state-of-the-art multispectral imaging methods are conducted.

5.1. Experiments on Synthetic Data

We test the proposed method on the Columbia Multispectral Image Database (CMID) [35] to verify the effectiveness, build a prototype spectrometer and further demonstrate our method on real captured data.

Quantitative Comparisons with State-of-the-art Methods. We first test the proposed method on the dataset and compare the PSNR with state-of-the-art compressive snapshot multispectral imagers, i.e. SD-CASSI [29], DD-CASSI [17]. Considering our system actually requires two kinds of projections, i.e., the sharp gray projection and the dispersive blurred projection, we also compare the performance with the hybrid version of SD-CASSI and DD-CASSI, i.e. hybrid SD-CASSI and hybrid DD-CASSI, and hybrid PMIS [7, 30] for fair comparison. Fig. 3 shows the

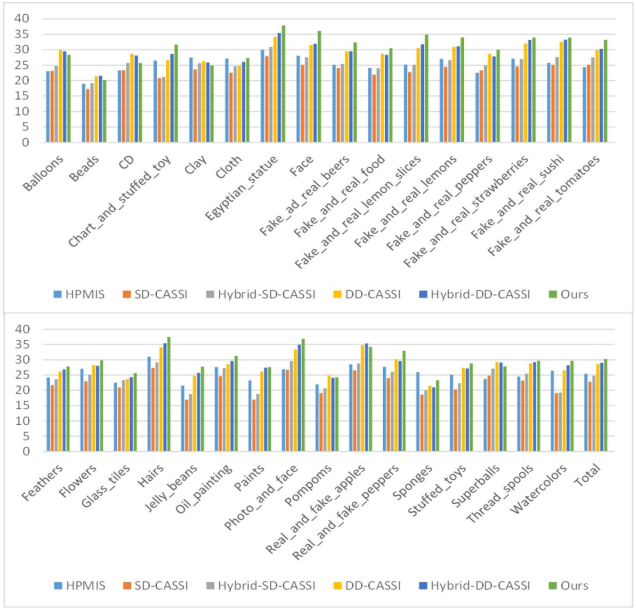

Figure 3. Quantitative comparisons with state-of-the-art multispectral imaging methods on hyperspectral dataset [35].

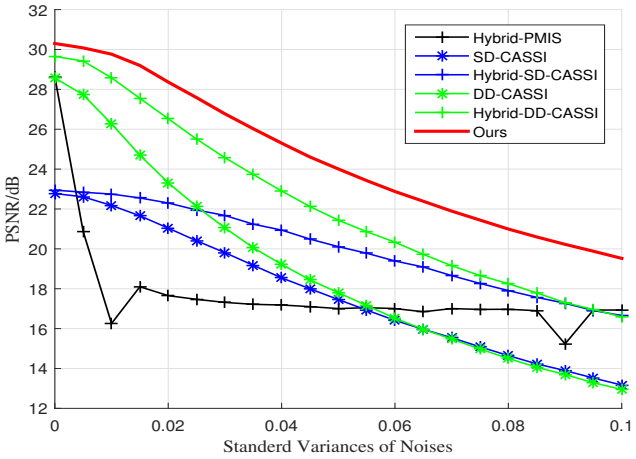

Figure 4. Comparison on different noise levels with state-of-the-art multispectral imagers.

Peak Signal to Noise Ratio (PSNR) of the results of proposed method and other state-of-the-art methods. We can see that the reconstruction quality of proposed method is comparable or even better than the state-of-the-art spectral imaging method. Besides, the proposed method performs slightly worse than other methods on the images containing invalid cases of our assumptions, like the Balloons scene which contains severe specular highlight effects. As for the cases coincided with the assumptions, the proposed method can achieve better performance, showing the great potential of proposed method in hyperspectral imaging.

Performance Comparison with Different Noise Levels. We also apply the proposed method on different noise lev-

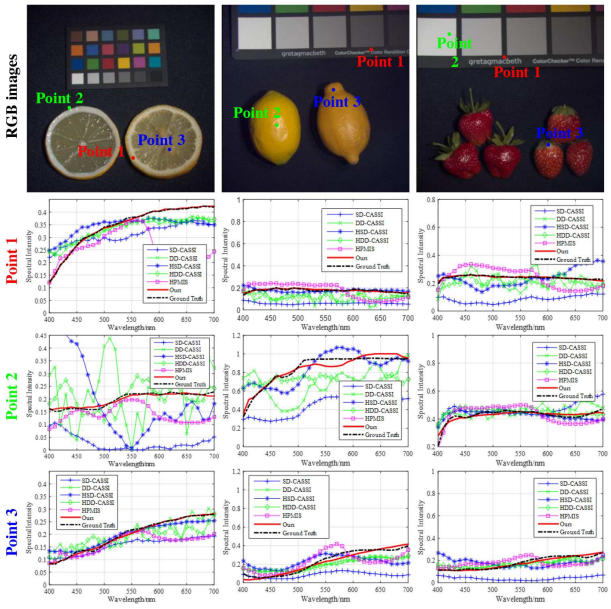

Figure 5. Spectral reconstruction results comparisons of the proposed and state-of-the-art methods. Curves extracted from three multispectral images (i.e. 'lemon_slices_ms', 'lemons_ms' and 'real_and_fake_strawberries_ms') from CMID [35] are presented. Three selected points of each image are marked in the RGB images (top row), and the corresponding spectral curves of the Point 1, 2 and 3 are shown in second to bottom rows respectively.

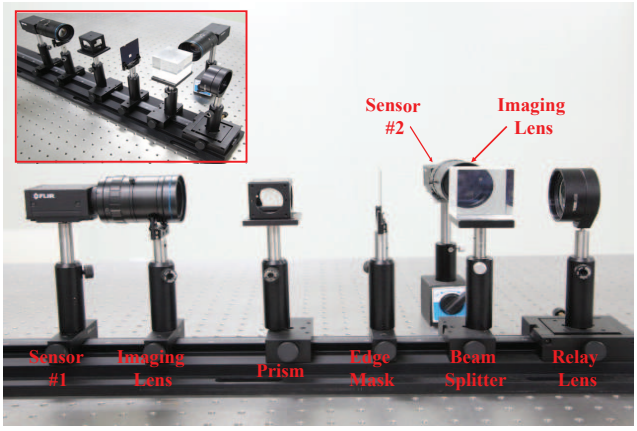

Figure 6. The prototype spectrometer: front view and side view.

els to test the noise tolerance of our method, and compare it with other multispectral imaging methods. As shown in Fig. 4, the degrading trend of the performance of our method is much slower than that of DD-CASSI based methods, showing the excellent capablility of noise resistance of our method. Especially for the hybrid-DD-CASSI method, which performs comparable with our method on noise free data, the recovery performance degrades rapidly with the increase of noise. In contrast, the SD-CASSI and hybrid-SD-CASSI present good noise tolerance in the experiments, so that their results become better or comparable than DD-CASSI and hybrid-DD-CASSI when noise level is larger.

It is worth noting that the proposed scheme can enhance the light throughput of the spectral imager, and thus decrease the noise level of observed measurements as well. In other words, under the same illumination condition, the measurements of our proposed system can achieve higher SNR than other hybrid state-of-the-art snapshot multispectral imagers. Considering the proposed method achieves comparable or even better performance in noise tolerance experiment, as shown in Fig. 4, our method is of great potential in the light-starved applications [20, 32, 34], which is a common case in most multispectral imaging scenarios.

We present the reconstructed spectral curves of proposed and state-of-the-art methods on the images from CMID [35], as shown in Fig. 5. Compared with the other three spectral imaging methods, the proposed method achieves much higher accuracy.

5.2. Experiments on Real Captured Data

We build the prototype spectral imager as in Fig. 6, and reconstruct real captured spectral images with the proposed algorithm. As for the calibration step, since the prism disperser which leads to nonlinear dispersion is used in our system, we pre-calibrate the non-linear dispersion, and correct the reconstructed spectral curves with the calibration results. The prism can introduce additional anisotropy aberrations, which may deteriorate the quality of our imaging system. This is a common problem of prism-based spectrometers, and can be greatly alleviated by adopting Amici prism (exactly what we use). The reconstruction results are shown in Fig. 7. The 1st column is the captured dispersive image and the second column is the captured sharp gray image. We reconstruct the multispectral images from these two measurements. Based on the reconstructed multispectral images, we calculate the corresponding RGB images and compare with the captured RGB images. The results are shown in the 3th-4th column. As shown, our result resembles the captured RGB images, demonstrating the high quality of our results. Further, the reconstructed images at 480 nm, 540 nm, 620 nm, 650 nm and the corresponding detailed region are shown in the 5th-8th column. As shown in column 7 and 8, our method could recover the spatial details, further verifying the proposed algorithm on the retrieving ability of spatial resolution. The ground truth here is captured by an RGB camera. Accurately calibrating its characteristics, e.g., the white balance, the spectral transmission of optical lenses and the spectral response curves of its RGB sensor, is difficult in practice and the inaccuracy may cause slight color difference between captured images and our results. Furthermore, to check the reconstruction quality directly, we use a single point spectrometer to capture the ground truth spectra of points in the scene and com-

pare with our method. The scene illumination is a tungsten lamp and as compared, our results resemble the captured spectrum from the single point spectrometer, verifying the effectiveness of our method.

6. Discussion and Conclusion

In this paper, we propose a novel view of the multispectral imaging problem. By exploring the dispersive blur between adjacent regions in dispersive blurred images, we propose to reconstruct the spectral images from the DoB constraints. A graph model is introduced to describe the linear equation system consisting of DoB constraints. Based on the graph model, we prove the most important conclusion of this paper, i.e., the whole spectral image can be reconstructed from a single dispersive blurred image and the spectrum of a single point. Based on the theory, we build an effective spectral imaging method. The proposed method have the following advantages: (1) Without using modulation, the proposed spectral imaging method is simple, easy to calibrate and low cost, promising for wider applications. (2) The light throughput can be flexibly tuned through adjusting the splitting ratio of light between the two arms with different beamsplitters, so that the spectral imager can approach very high light throughput (70%-80%).

As for future work, there are a few interesting topics that are worth to explore, such as directly estimating the edge information from the dispersive blurred image, further modeling the specularities and complex illumination conditions, introducing perpendicular dispersion pairs for anisotropy reduction.

Acknowledgement.

This work was supported by Grant No.61671236 from National Science Foundation of China, Grant No. BK20160634 from National Science Foundation for Young Scholar of Jiangsu Province.

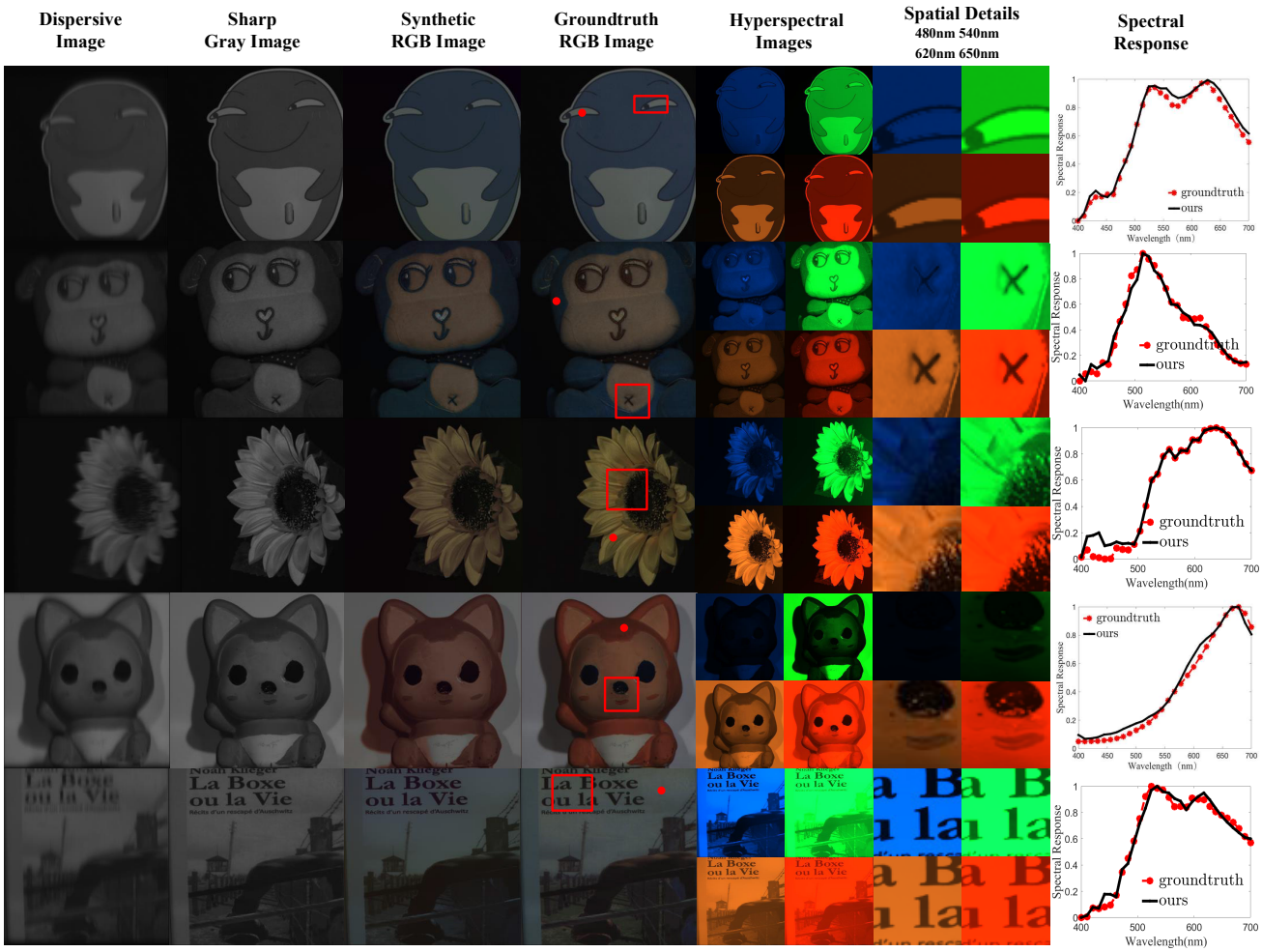

Figure 7. Experimental results on real captured data. The synthetic RGB images, spatial details and spectral responses at marked dots are evaluated.

References

[1] B. Arad and O. Ben-Shahar. Sparse recovery of hyperspectral signal from natural rgb images. In *Proc. ECCV*, pages 19–34. Springer, 2016. 1, 2

[2] B. Arad and O. Ben-Shahar. Filter selection for hyperspectral estimation. In *Proc. CVPR*, pages 21–26, 2017. 1, 2

[3] V. Backman, M. Wallace, L. Perelman, J. Arendt, R. Gurjar, M. Müller, Q. Zhang, G. Zonios, E. Kline, T. McGillican, et al. Detection of preinvasive cancer cells. *Nature*, 406(6791):35–36, 2000. 1

[4] S.-H. Baek, I. Kim, D. Gutierrez, and M. H. Kim. Compact single-shot hyperspectral imaging using a prism. *ACM Trans. on Graphics (TOG)*, 36(6):217, 2017. 1, 2

[5] J. Bao and M. G. Bawendi. A colloidal quantum dot spectrometer. *Nature*, 523(7558):67, 2015. 1, 2

[6] R. W. Basedow, D. C. Carmer, and M. E. Anderson. Hydice system: Implementation and performance. In *Proc. SPIE*, pages 258–267, 1995. 2

[7] X. Cao, X. Tong, Q. Dai, and S. Lin. High resolution multispectral video capture with a hybrid camera system. In *Proc. CVPR*, pages 297–304, 2011. 1, 2, 4, 6

[8] W. Debskia, P. Walczykowskia, A. Klewskia, and M. Zyznowskib. Analysis of usage of multispectral video technique for distinguishing objects in real time. In *ISPRS*, 2004. 1

[9] M. Descour and E. Dereniak. Computed-tomography imaging spectrometer: experimental calibration and reconstruction results. *Appl. Opt.*, 34(22):4817–4826, 1995. 1, 2

[10] Y. Fu, T. Zhang, Y. Zheng, D. Zhang, and H. Huang. Joint camera spectral sensitivity selection and hyperspectral image recovery. In *Proc. ECCV*, pages 812–828. Springer, 2018. 1, 2

[11] Y. Fu, Y. Zheng, I. Sato, and Y. Sato. Exploiting spectral-spatial correlation for coded hyperspectral image restoration. In *Proc. CVPR*, pages 3727–3736, 2016. 1, 2

[12] B. Funt and J. Ho. Color from black and white. *IJCV*, 3(2):109–117, 1989. 1, 3

[13] L. Gao, R. T. Kester, and T. S. Tkaczyk. Compact image slicing spectrometer (iss) for hyperspectral fluorescence microscopy. *Opt. Express*, 17(15):12293–12308, 2009. 1, 2

[14] L. Gao, J. Liang, C. Li, and L. V. Wang. Single-shot compressed ultrafast photography at one hundred billion frames per second. *Nature*, 516(7529):74, 2014. 2

[15] N. Gat. Imaging spectroscopy using tunable filters: a review. In *Wavelet Applications VII*, volume 4056, pages 50–65. International Society for Optics and Photonics, 2000. 2

[16] N. Gat, G. Scriven, J. Garman, M. De Li, and J. Zhang. Development of four-dimensional imaging spectrometers (4d-is). In *Proc. SPIE*, pages 63020M–63020M, 2006. 1, 2

[17] M. Gehm, R. John, D. Brady, R. Willett, and T. Schulz. Single-shot compressive spectral imaging with a dual-disperser architecture. *Opt. Express*, 15(21):14013–14027, 2007. 1, 2, 6

[18] N. A. Hagen, L. S. Gao, T. S. Tkaczyk, and R. T. Kester. Snapshot advantage: a review of the light collection improvement for parallel high-dimensional measurement systems. *Opt. Eng.*, 51(11):111702, 2012. 2

[19] F. Heide, M. Rouf, M. B. Hullin, B. Labitzke, W. Heidrich, and A. Kolb. High-quality computational imaging through simple lenses. *ACM Transactions on Graphics (TOG)*, 32(5):149, 2013. 5

[20] W. Jahr, B. Schmid, C. Schmied, F. O. Fahrbach, and J. Huisken. Hyperspectral light sheet microscopy. *Nature Commu.*, 6:7990, 2015. 2, 7

[21] J. Jia, K. J. Barnard, and K. Hirakawa. Fourier spectral filter array for optimal multispectral imaging. *IEEE Trans. on Image Process.*, 25(4):1530–1543, 2016. 1, 2

[22] P. J. Lapray, X. Wang, J. B. Thomas, and P. Gouton. Multispectral filter arrays: Recent advances and practical implementation. *Sensors*, 14(11):21626–21659, 2014. 1, 2

[23] X. Lin, Y. Liu, J. Wu, and Q. Dai. Spatial-spectral encoded compressive hyperspectral imaging. *ACM Trans. on Graph.*, 33(6):233, 2014. 1, 2

[24] K. Mitra, O. S. Cossairt, and A. Veeraraghavan. A framework for analysis of computational imaging systems: role of signal prior, sensor noise and multiplexing. *IEEE Trans. Pattern Anal. Mach. Intell.*, 36(10):1909–1921, 2014. 1

[25] S. Nie, L. Gu, Y. Zheng, A. Lam, N. Ono, and I. Sato. Deeply learned filter response functions for hyperspectral reconstruction. In *Proc. CVPR*, pages 4767–4776, 2018. 1, 2

[26] Z. Pan, G. Healey, M. Prasad, and B. Tromberg. Face recognition in hyperspectral images. *IEEE Trans. Pattern Anal. Mach. Intell.*, 25(12):1552–1560, 2003. 1

[27] W. M. Porter and H. T. Enmark. A system overview of the airborne visible/infrared imaging spectrometer (aviris). In *31st Ann. Tech. Sym.*, pages 22–31. International Society for Optics and Photonics, 1987. 2

[28] A. Wagadarikar, R. John, R. Willett, and D. Brady. Single disperser design for coded aperture snapshot spectral imaging. *App. Opt.*, 47(10):B44–B51, 2008. 1, 2

[29] A. a. Wagadarikar, N. P. Pitsianis, X. Sun, and D. J. Brady. Video rate spectral imaging using a coded aperture snapshot spectral imager. *Opt. Express*, 17(8):6368–6388, 2009. 6

[30] L. Wang, Z. Xiong, D. Gao, G. Shi, and F. Wu. Dual-camera design for coded aperture snapshot spectral imaging. *Appl. Opt.*, 54(4):848–858, Feb 2015. 1, 2, 6

[31] L. Wang, Z. Xiong, D. Gao, G. Shi, W. Zeng, and F. Wu. High-speed hyperspectral video acquisition with a dual-camera architecture. In *Proc. CVPR*, pages 4942–4950, 2015. 2

[32] J. Wu, B. Xiong, X. Lin, J. He, J. Suo, and Q. Dai. Snapshot hyperspectral volumetric microscopy. *Sci. Rep.*, 6:24624, 2016. 2, 7

[33] S. Wug Oh, M. S. Brown, M. Pollefeys, and S. Joo Kim. Do it yourself hyperspectral imaging with everyday digital cameras. In *Proc. CVPR*, pages 2461–2469, 2016. 1, 2

[34] Z. Xiong, L. Wang, H. Li, D. Liu, and F. Wu. Snapshot hyperspectral light field imaging. In *Proc. CVPR*, volume 2, 2017. 2, 7

[35] F. Yasuma, T. Mitsunaga, D. Iso, and S. K. Nayar. Generalized assorted pixel camera: postcapture control of resolution, dynamic range, and spectrum. *IEEE Trans. on Image Process.*, 19(9):2241–2253, 2010. 6, 7

[36] T. Yue, J. Suo, J. Wang, X. Cao, and Q. Dai. Blind optical aberration correction by exploring geometric and visual priors. In *Proc. CVPR*, pages 1684–1692, 2015. 6